

Flux-pinning mechanism in silicone-oil-doped MgB₂: Evidence for charge-carrier mean free path fluctuation pinning

S. R. Ghorbani,^{1,2} X. L. Wang,^{1,*} S. X. Dou,¹ Sung-IK Lee,^{3,†} and M. S. A. Hossain¹

¹*Institute for Superconducting and Electronic Materials, University of Wollongong, Wollongong, New South Wales 2522, Australia*

²*Department of Physics, Tarbiat Moallem University of Sabzevar, P.O. Box 397, Sabzevar, Iran*

³*Department of Physics, National Creative Research Initiative Center for Superconductivity, Sogang University, Seoul 121-742, Republic of Korea*

(Received 5 March 2008; revised manuscript received 12 August 2008; published 3 November 2008)

Flux-pinning mechanism of MgB₂ doped with 10 wt % silicone-oil sintered at low and high temperatures has been investigated by magnetic measurements. The field dependence of the critical current density, $j_c(B)$, was analyzed within the collective pinning model. A crossover field, B_{sb} , from the single vortex to the small vortex bundle-pinning regime was observed. For both types of sintered samples, the temperature dependence of $B_{sb}(T)$ at low temperature is in good agreement with the δl pinning mechanism, i.e., pinning associated with charge-carrier mean free path fluctuation. At temperatures close to the critical temperature, however, there is evidence for δT_c pinning, which is associated with spatial fluctuations of the transition temperature. These results provide strong evidence that the liquid precursor, silicone oil, produces very small pinning centers and enhances the $j_c(B)$.

DOI: [10.1103/PhysRevB.78.184502](https://doi.org/10.1103/PhysRevB.78.184502)

PACS number(s): 74.70.Ad, 74.25.Qt, 74.25.Sv

I. INTRODUCTION

Magnesium diboride MgB₂ has the highest superconducting transition temperature ($T_c \approx 39$ K)¹ among the metallic compounds. The critical current density has been a central topic of research since discovery of superconductivity in this compound. High critical current-density values of 10^5 – 10^6 A/cm² have been reported for this superconductor. However, the critical current density drops rapidly with increasing magnetic field due to its poor flux pinning. At the irreversibility field, H_{irr} , vortices start to move along the direction of the current flow, and hence the critical current vanishes. The current-density decay behavior is governed by the pinning mechanism. Numerous studies have been performed with the purpose of understanding the vortex-pinning mechanisms^{2–10} that are responsible for improving the critical current density, j_c . Intergrain boundary pinning⁸ and point defect pinning⁵ are two main important pinning mechanisms.

In type-II superconductors, the most important elementary interaction between vortices and pinning centers is the magnetic interaction and the core interaction. The core interaction arises from the coupling of the locally distorted superconducting properties with the periodic variation in the superconducting order parameter, which is usually more effective in type-II superconductors due to the high k value.

It has been found that in MgB₂ bulk and thin-film samples, with κ larger than 20,^{11,12} the core pinning is related to randomly distributed spatial variations in the transition temperature (δT_c pinning).^{6,13} However, in the high-temperature superconductors the core interaction is associated with charge-carrier mean free path variations (δl pinning), mostly due to crystal lattice defects.¹⁴

The critical current density of MgB₂ can be improved by more than 1 order of magnitude in high magnetic field by adding nano-SiC.¹⁵ It has also been found that maximum

flux-pinning forces are increased by decreasing grain size.¹⁶ One way to decrease the grain size is to use a liquid precursor, silicone oil, which can produce Si and C at the atomic scale.¹⁷ We have found that a significant flux-pinning enhancement in MgB₂ can be easily achieved in this way. Our results showed that the Si and C released from the decomposition of the silicone oil formed Mg₂Si and substituted into B sites, respectively. The inclusion of the silicone oil leads to a reduction in the lattice parameters, as well as T_c and the relative resistance ratio (RRR) [$R(300\text{ K})/R(T_c)$] resulting in a significant enhancement of $J_c(H)$, H_{irr} , and H_{c2} .

Due to the defects and nanoparticle inclusions related J_c -field enhancement in the silicone-oil doped MgB₂, the pinning mechanisms are of interest in such samples from the point of view of both the fundamental physics and applications. However, it has not been experimentally determined whether the δT_c pinning or the δl pinning is the dominant mechanism in MgB₂ when it is doped on the atomic scale.

In this paper, the vortex-pinning mechanisms of silicone-oil-doped samples are discussed in the framework of the collective theory. It was found that charge-carrier mean free path fluctuation pinning (δl) is the only important pinning mechanism at low temperature, while δT_c pinning is effective at T close to T_c .

II. EXPERIMENTAL

Polycrystalline MgB₂ samples with 10 wt % silicone-oil addition were prepared by the standard solid-state powder processing technique, which has been well described elsewhere.¹⁷ Because the grain size of MgB₂ also plays an important role in governing the flux pinning, we fabricated silicone-oil-doped MgB₂ at both 600 and 900 °C with the aim of achieving small and large grains of MgB₂, respectively. Although x-ray diffraction (XRD) results revealed that all samples were crystallized in the MgB₂ structure as the

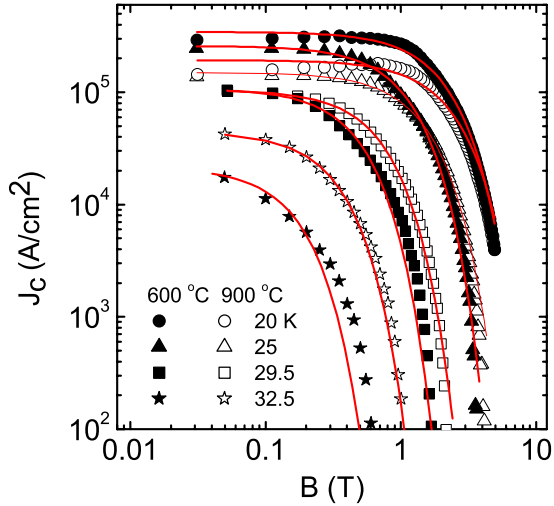


FIG. 1. (Color online) Magnetic and temperature dependences of the critical current density j_c for 600 and 900 °C reaction temperatures. The solid curves are fits to Eq. (2).

major phase, a few impurity lines of MgO and Mg₂Si were observed.

Magnetic and transport measurements were performed using a physical properties measurement system (PPMS) (Quantum Design). The magnetic hysteresis loops of the samples were measured over a temperature range of 20–34 K for both samples. The critical current density was calculated by using the Bean approximation, $j_c = 20\Delta M/Va(1-a/3b)$, where a and b are the width and the length of the sample perpendicular to the applied field, respectively, V is the sample volume, and ΔM is the height of the M - H hysteresis loop.

III. RESULTS AND DISCUSSIONS

The $j_c(B, T)$ results for both samples sintered at 600 and 900 °C are shown in a double-logarithmic plot in Fig. 1. At 4 T and 20 K, the j_c values for both samples are over 1×10^4 A/cm², more than 1 order of magnitude higher than that for pure MgB₂.¹⁷ This is due to enhancement of flux pinning, which may be ascribed to the fine nanoparticles, mainly Mg₂Si, C, and MgO, which occur as inclusions inside MgB₂ grains. The j_c initially shows a plateau at low field and then begins to decrease quickly as the field reaches a cross-over field, which is decreased with increasing temperature. Further increase in the field results in a faster drop in j_c near the irreversibility line, which is obtained by using the criterion of $j_c = 100$ A/cm², as shown in Fig. 2.

For all fields and temperatures higher than 29.5 K, the critical current density of samples sintered at 900 °C is higher than those sintered at the 600 °C. This is in agreement with the higher B_{c2} (see Fig. 2) and the increased grain connectivity resulting from the higher-temperature reaction. At low magnetic fields and temperatures, samples sintered at 600 °C have higher j_c values than that sintered at 900 °C. This results is surprising but is consistent with the SiC-doped MgB₂.¹⁸ Grain boundary pinning may also play a role because it is usually important at low field region as seen in undoped MgB₂.¹⁹

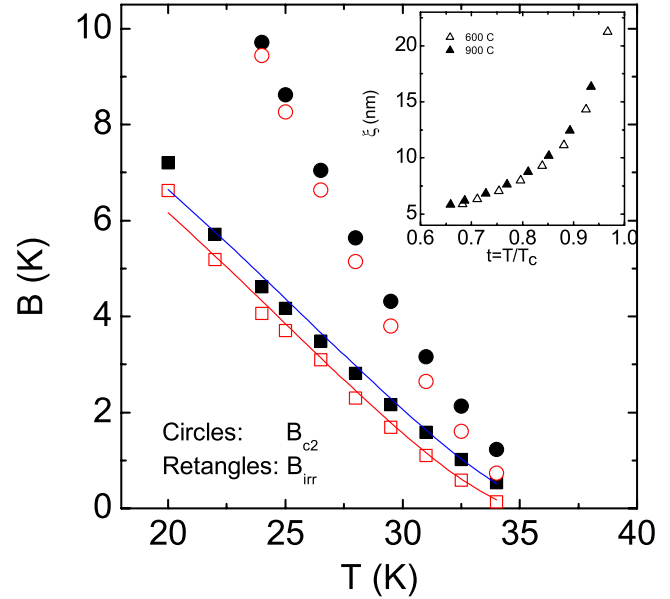


FIG. 2. (Color online) The upper critical and irreversibility fields of the 10 wt % silicone-oil-doped MgB₂ as a function of temperature for two different sintering reaction temperatures. The solid curves are fits to $B_{irr} = B_{irr}(0)[1 - (T/T_c)^2]^{3/2}$ with fitting parameter $B_{irr}(0)$. Inset: The coherence length ξ of silicone-oil-doped MgB₂ as function of the normalized temperature T/T_c and the reaction temperature. Open symbols: 600 °C. Solid symbols: 900 °C.

The temperature dependence of the upper critical fields, B_{c2} , which is obtained from the 90% values of their corresponding resistivity transitions, are shown in Fig. 2. As typically reported,¹¹ the B_{c2} curve shows a slight upward curvature close to T_c for both sintering temperatures, and it increases with increasing temperature of the reaction. The solid curves in Fig. 2 are in close agreement with the typical behavior expected in the case of giant flux creep, which is predicted from the $(1-t^2)^{3/2}$ (where $t = T/T_c$) behavior for B_{irr} .²⁰ By extrapolating the B_{c2} - T curves to zero temperature, we found $B_{c2}(10$ K) to be about 28.04 and 31.5 T for the 600 and 900 °C reaction temperatures, respectively. These results are in good agreement with $B_{c2}(10$ K) of 10% nano-SiC-doped bulk MgB₂ samples.²¹ This fact further indicates that the silicone-oil doping is a very effective and cheap dopant¹⁷ which produces excellent j_c field dependence at the same level as state-of-the-art nano-SiC-doped MgB₂.

The coherence length, ξ , can be calculated from the $\xi(T) = [\varphi_0/2\pi B_{c2}(T)]^{1/2}$ relation at different temperatures, where φ_0 is the magnetic-flux quantum. $\xi(T)$ results as a function of the normalized temperature T/T_c and the reaction temperature are shown in the inset of Fig. 3. The ξ of the MgB₂ sintered at 600 °C is slightly larger than that of the 900 °C MgB₂. However, the decreasing trends are same for both reaction temperatures.

In order to understand the critical current-density results shown in Fig. 1, the pinning force $F_p = B \times j_c$ was calculated. The scaling behavior for the normalized volume pinning force $f_p = F_p/F_{p,max}$, was examined for both $h_1 = B/B_{irr}$ and $h_2 = B/B_{max}$, where B_{max} is the magnetic field at the maximum of F_p . The results are shown in Fig. 3. The $f_p(h_2)$ curve

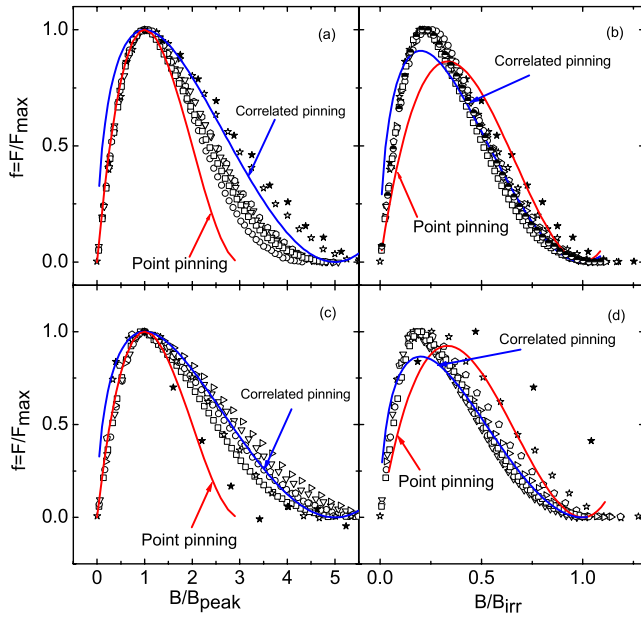


FIG. 3. (Color online) Magnetic dependence of the reduced pinning force $f(h)$ at a temperature range of 20–34 K. (a) $h_2 = B/B_{\max}$ for the 900 °C sintered sample, (b) $h_1 = B/B_{\text{irr}}$ for the 900 °C sintered sample, (c) $h_2 = B/B_{\max}$ for the 600 °C sintered sample, and (d) $h_1 = B/B_{\text{irr}}$ for the 600 °C sintered sample. Solid curves are fittings to two different types of point pinning centers. The dashed curves represent $f_p(h_1) = 7.57h_1^{0.9}(1-h_1)^{2.9}$ and $f_p(h_1) = 9.47h_1^{1.01}(1-h_1)^{2.9}$ for the 600 and 900 °C samples, respectively.

does not exhibit scaling behavior at higher temperatures. Otherwise, scaling was achieved by fitting with normal point pinning, $f(h_2) = (9/4)h_2(1-h_2/3)^2$, and correlated pinning, $f(h_2) = (25/16)h_2^{0.5}(1-h_2/5)^2$, which was inferred by Higuchi *et al.*²² The fitting results are shown by solid curves in the Figs. 3(a) and 3(c). In lower fields, the experimental data are in good agreement with the point pinning mechanism for both reaction temperatures. At normalized magnetic fields larger than $h_{2\max}$, flux pinning is dominated by correlated pinning for the sample sintered at 600 °C at temperatures lower than 34 K, while at $T \geq 34$ K, point pinning is dominant. For the 900 °C sample at temperatures lower than 32.5 K, the experimental data are located between the theoretical curves for correlated pinning and point pinning. Therefore, we cannot obtain any dominant pinning mechanism. In another sort of scaling behavior, the $f_p(h_1)$ at $T < 29.5$ K for the 600 °C sample and $T < 34$ K for the 900 °C sample exhibits scaling behavior.

For the scaling, a common law of $f_p(h_1) = Ah_1^p(1-h_1)^q$ is usually employed as a single pinning function, where p and q are parameters describing the pinning mechanism.²³ In this model, $p = 1/2$ and $q = 2$ describe normal core correlated pinning, while $p = 1$ and $q = 2$ describe normal core point pinning, as was predicted by Kramer.²⁴ The best fit of the curves [solid curves in Figs. 3(b) and 3(d)] are obtained with ($p = 0.9$ and $q = 2.9$) and ($p = 1.01$ and $q = 2.9$) for 600 and 900 °C reaction temperatures, respectively. Therefore, we cannot infer the real dominant pinning mechanism from this scaling behavior.

As mentioned before, the j_c of both samples shows at least one crossover field, such as B_{sb} . In the framework of the

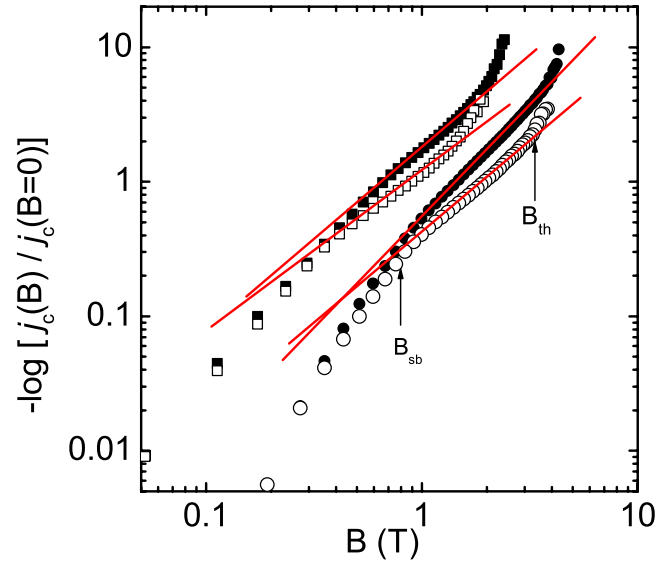


FIG. 4. (Color online) Double logarithmic plot of $-\log[j_c(B)/j_c(0)]$ as a function of B at $T = 25$ (circles) and 29.5 K (rectangles) for the samples sintered at 600 (open symbols) and 900 °C (solid symbols). The crossover fields B_{sb} and B_{th} are shown by arrows for one sample at 25 K.

collective theory, which was derived by Blatter *et al.*,²⁰ the critical current density is field independent when the applied magnetic field is lower than the crossover field. In the regime below B_{sb} a single vortex-pinning mechanism governs the vortex lattice,

$$B_{sb} \alpha j_{sv} B c_2, \quad (1)$$

where j_{sv} is the critical current density in the single vortex-pinning regime. At higher fields, for $B > B_{sb}$, $j_c(B)$ decreases quickly, and it follows an exponential law,

$$j_c(B) \approx j_c(0) \exp[-(B/B_0)^{3/2}], \quad (2)$$

where B_0 is a normalization parameter of the order of B_{sb} . For $B > B_{lb}$, a power dependence in the form of $j_c(B) \propto B^{-\beta}$ acts from B_{sb} to another crossover field B_{lb} (large bundle-pinning regime).

The experimental results shown in Fig. 1 for $j_c(B)$ can be described in terms of Eq. (2). The solid curves in Fig. 1 illustrate the fits to the collective model according to Eq. (2) with fitting parameters for $j_c(0)$ and B_0 . For clarification, $-\log[j_c(B)/j_c(0)]$ as a function of B is shown in a double-logarithmic plot in Fig. 4. It is clear that Eq. (2) well describes the experimental data for intermediate fields, while deviations from the fitting curves can be observed at both low and high fields. The deviation at low fields, below B_{sb} , is associated with crossover from the single vortex-pinning regime to the small bundle-pinning regime. The high-field deviation that is very close to the irreversibility line could be related to large thermal fluctuations,⁶ a view that is supported by the three-dimensional (3D) flux creep dependence observed for the variation in $B_{\text{irr}}(T)$ in Fig. 2. The field of this deviation is denoted as B_{th} . The large-bundle pinning does not fit our data. Above this field, vortex will become very soft and then H - T diagram will enter to the very narrow

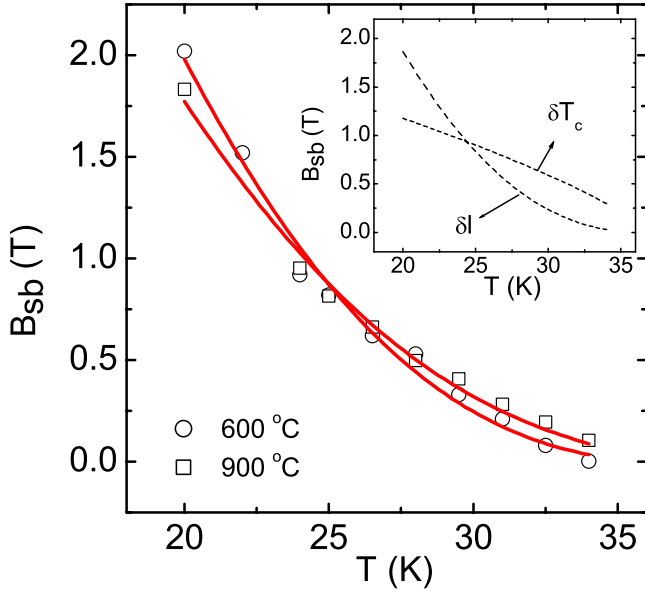


FIG. 5. (Color online) Temperature dependence of the crossover field B_{sb} . The solid curves are fits to Eq. (4). Inset: The δT_c and δl pinning curves correspond to Eq. (3).

thermal vortex region, in which vortex is thermally activated, but not enough to become a vortex liquid.

The crossover field B_{sb} as a function of temperature is shown in Fig. 5 for the samples sintered at 600 and 900 °C. As can be seen in Fig. 5, the crossover field B_{sb} is almost the same for both reaction temperatures. Therefore, B_{sb} is not sensitive to the reaction temperature. However, the $B_{th}(T)$ is dependent on the reaction temperature and increases with increasing sintering temperature (see Fig. 7).

Grissen *et al.*¹⁴ pointed out that the δT_c and δl pinning mechanisms result in different temperature dependencies of the critical current density j_{sv} in the single vortex-pinning regime. They found that $j_{sv} \propto (1-t^2)^{7/6}(1+t^2)^{5/6}$, with $t = T/T_c$, for the case of δT_c pinning, while for δl pinning, $j_{sv} \propto (1-t^2)^{5/2}(1+t^2)^{-1/2}$. Inserting these two $j_{sv}(T)$ expressions into Eq. (1), the following temperature dependence for B_{sb} can be obtained:⁶

$$B_{sb}(T) = B_{sb}(0) \left(\frac{1-t^2}{1+t^2} \right)^{\nu}, \quad (3)$$

where $\nu=2/3$ and 2 for δT_c and δl pinning, respectively. In the inset of Fig. 5, the dashed curves indicate the δT_c and δl pinning mechanisms, respectively. The curve has a positive curvature in the δT_c pinning case, while the curvature associated with the δl pinning is negative. As is clear from Fig. 5, the $B_{sb}(T)$ behavior shows a negative curvature. There is also a good agreement between our experimental points and Eq. (3) with $\nu=2$, and that strongly suggests that the δl pinning mechanism is dominant, especially in low temperatures.

To investigate further the real pinning mechanism of the silicone-oil-doped MgB_2 samples, the B_{sb} data was analyzed within the following expression:

$$B_{sb} = P_1 B_{sb}^{T_c} + P_2 B_{sb}^l, \quad (4)$$

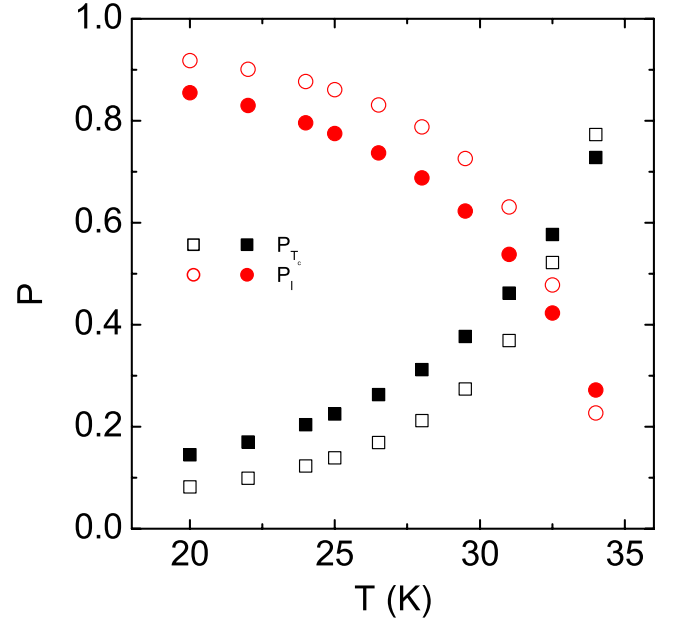


FIG. 6. (Color online) δT_c and δl pinning contributions as functions of temperature. Open symbols: 600 °C. Solid symbols: 900 °C.

where $B_{sb}^{T_c}$ and B_{sb}^l are the expression for δT_c and δl pinning, respectively. P_1 and P_2 are fitting parameters with $P_1 + P_2 = 1$. The B_{sb} data obtained from $j_c(B)$ was well described by Eq. (4), as shown by the solid curves in Fig. 5. In order to compare the effects of the δT_c and the δl pinning mechanisms, the P parameter was defined as $P = P_1 B_{sb}^{T_c} / B_{sb}$ or $P = P_2 B_{sb}^l / B_{sb}$, which represent δT_c or δl pinning effects, re-

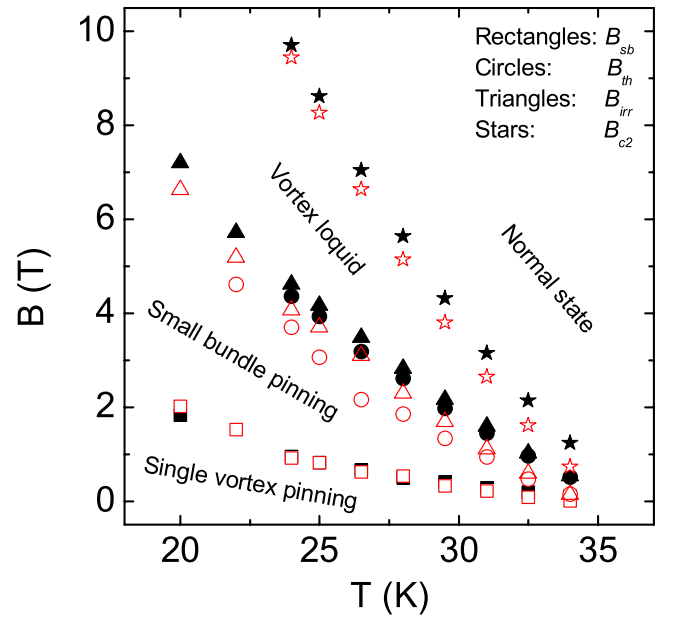


FIG. 7. (Color online) 10 wt % silicone-oil-doped MgB_2 phase diagram. B_{sb} and B_{th} were obtained from the experimental $j_c(B)$ data (see Fig. 4). $B_{irr}(T)$ and $B_{c2}(T)$ were obtained from the criterion $j_c = 100$ A/cm² and the 90% values of their corresponding resistivity transitions, respectively. Open symbols: 600 °C. Solid symbols: 900 °C.

spectively. The results of both pinning effect contributions are shown in Fig. 6. For both the 600 and 900 °C reaction temperatures, the trends in both δT_c pinning and δl pinning are the same, while the actual values of the pinning contribution are slightly different. As can be seen in Fig. 6, δl pinning is the dominant mechanism at low temperature but with increasing temperature, δl pinning decreases, and δT_c pinning increases. At $T \approx 31-32$, both pinning mechanisms have equal effects, and above these temperatures, δT_c pinning is the dominant.

Using the derived crossovers B_{sb} and B_{th} , the reconstructed B - T phase diagram is shown in Fig. 7. According to the collective pinning model,²⁰ the disorder-induced spatial fluctuations in the solid-vortex lattice can be clearly divided into markedly different regimes according to the strength of the applied field. Three different regimes are at least distinguishable: (1) single vortex pinning, which governs the region below B_{sb} ; (2) small bundle pinning, which holds between B_{sb} and B_{th} ; (3) the region between B_{th} and B_{irr} , where thermal fluctuations are important; and (4) vortex liquid region. The comparison with the phase diagram of a pure MgB₂ bulk sample⁶ shows quite different trends and areas of the each vortex phases. The silicone-oil-doped MgB₂

samples show very wide regions of the vortex phases, which originate from the vastly enhanced vortex pinning. Especially at low temperature, each curve exhibits upward curvature which indicates even stronger pinning behavior at low temperature.

In conclusion, we have found that the δl pinning mechanism due to spatial fluctuations of the charge-carrier mean free path is strongly dominant at low temperature in MgB₂ that was doped with silicone oil and sintered at both 600 and 900 °C, while at temperatures close to the critical temperature, δT_c pinning is effective. The field-temperature phase diagram shows at least three different vortex-pinning regimes in the solid-vortex lattice region.

ACKNOWLEDGMENTS

This work was supported by the Australian Research Council through ARC discovery and International Linkage projects, and the Superconductivity Center of Sogang University through the program of Acceleration research of MOST and/or KOSEF of Korea and special fund of Sogang University.

*xiaolin@uow.edu.au

†silee77@sogang.ac.kr

¹G. J. Nagamatsu, N. Nakagawa, T. Muranaka, Y. Zenitali, and J. Akimitsu, *Nature* (London) **410**, 63 (2001).

²C. Larbalestier, M. O. Rikel, L. D. Cooley, A. A. Polyanskii, J. Y. Jiang, S. Patnaik, X. Y. Cai, D. M. Feldmann, A. Gurevich, A. A. Squitieri, M. T. Naus, C. B. Eom, E. E. Hellstrom, R. J. Cava, K. A. Regan, N. Rogado, M. A. Hayward, T. He, J. S. Slusky, P. Khalifah, K. Inumaru, and M. Haas, *Nature* (London) **410**, 186 (2001).

³H.-J. Kim, W. N. Kang, E.-Mi Choi, M.-S. Kim, K. H. P. Kim, and S.-I. Lee, *Phys. Rev. Lett.* **87**, 087002 (2001).

⁴M.-S. Kim, C. U. Jung, M.-S. Park, S. Y. Lee, K. H. P. Kim, W. N. Kang, and S.-I. Lee, *Phys. Rev. B* **64**, 012511 (2001).

⁵S. X. Dou, A. V. Pan, S. Zhou, M. Ionescu, X. L. Wang, J. Horvat, H. K. Liu, and P. R. Munroe, *J. Appl. Phys.* **94**, 1850 (2003); I. Pallecchi, C. Tarantini, H. U. Aebersold, V. Braccini, C. Fanciulli, C. Ferdeghini, F. Gatti, E. Lehmann, P. Manfrinetti, D. Marré, A. Palenzona, A. S. Siri, M. Vignolo, and M. Putti, *Phys. Rev. B* **71**, 212507 (2005).

⁶M. J. Qin, X. L. Wang, H. K. Liu, and S. X. Dou, *Phys. Rev. B* **65**, 132508 (2002).

⁷M. Xu, H. Kitazawa, Y. Takano, J. Ye, K. Nishida, H. Abe, A. Matsushita, and G. Kido, *Appl. Phys. Lett.* **79**, 2779 (2001).

⁸J. Wang, Z. X. Shi, H. Lv, and T. Tamegai, *Physica C* **445-448**, 462 (2006); J. Jung, I. Isaac, and M. A.-K. Mohamed, *Phys. Rev. B* **48**, 7526 (1993).

⁹K. H. P. Kim, J. H. Choi, C. U. Jung, P. Chowdhury, Hyun-Sook Lee, M. S. Park, H. J. Kim, J. Y. Kim, Z. Du, E. M. Choi, M. S. Kim, W. N. Kang, S. I. Lee, G. Y. Sung, and J. Y. Lee, *Phys. Rev. B* **65**, 100510(R) (2002).

¹⁰A. K. Pradhan, Z. X. Shi, M. Tokunaga, T. Tamegai, Y. Takano, K. Togano, H. Kito, and H. Ihara, *Phys. Rev. B* **64**, 212509

(2001).

¹¹C. Buzea and T. Yamashita, *Supercond. Sci. Technol.* **14**, R115 (2001).

¹²D. K. Finnemore, J. E. Ostenson, S. L. Bud'ko, G. Lapertot, and P. C. Canfield, *Phys. Rev. Lett.* **86**, 2420 (2001).

¹³S. L. Prischepa, M. L. Della Rocca, L. Maritato, M. Salvato, R. Di Capua, M. G. Maglione, and R. Vaglio, *Phys. Rev. B* **67**, 024512 (2003).

¹⁴R. Griessen, Wen Hai-hu, A. J. J. van Dalen, B. Dam, J. Rector, H. G. Schnack, S. Libbrecht, E. Osquiguil, and Y. Bruynseraede, *Phys. Rev. Lett.* **72**, 1910 (1994).

¹⁵S. X. Dou, S. Soltanian, J. Horvat, X. L. Wang, S. H. Zhou, M. Ionescu, H. K. Liu, P. Munroe, and M. Tomsic, *Appl. Phys. Lett.* **81**, 3419 (2002).

¹⁶E. Martínez, P. Mikheenko, M. Martínez-López, A. Millán, A. Bevan, and J. S. Abell, *Phys. Rev. B* **75**, 134515 (2007).

¹⁷X. L. Wang, Z. X. Cheng, and S. X. Dou, *Appl. Phys. Lett.* **90**, 042501 (2007).

¹⁸Y. Zhu, A. Matsumoto, B. J. Senkowicz, H. Kumakura, H. Kitaguchi, M. C. Jewell, E. E. Hellstrom, D. C. Larbalestier, and P. M. Voyles, *J. Appl. Phys.* **102**, 013913 (2007).

¹⁹H. Kitaguchi, A. Matsumoto, H. Kumakura, T. Doi, H. Sosiati, and S. Hata, *Appl. Phys. Lett.* **85**, 2842 (2004).

²⁰G. Blatter, M. V. Feigel'man, V. B. Geshkenbein, A. I. Larkin, and V. M. Vinokur, *Rev. Mod. Phys.* **66**, 1125 (1994).

²¹A. Matsumoto, H. Kumakura, H. Kitaguchi, B. J. Senkowicz, M. C. Jewell, E. E. Hellstrom, Y. Zhu, P. M. Voyles, and D. C. Larbalestier, *Appl. Phys. Lett.* **89**, 132508 (2006).

²²T. Higuchi, S. I. Yoo, and M. Murakami, *Phys. Rev. B* **59**, 1514 (1999).

²³D. Dew-Hughes, *Philos. Mag.* **30**, 293 (1974).

²⁴E. J. Kramer, *J. Appl. Phys.* **44**, 1360 (1973).